




Cite this: *CrystEngComm*, 2022, 24, 5801

# Rapid, energy-efficient and pseudomorphic microwave-induced-metal-plasma (MIMP) synthesis of $\text{Mg}_2\text{Si}$ and $\text{Mg}_2\text{Ge}^\dagger$

Zhen Fan,<sup>a</sup> Hsi-Nien Ho,<sup>b</sup> Robert Szczęśny,<sup>c</sup>  
Wei-Ren Liu <sup>b</sup> and Duncan H. Gregory <sup>\*,a</sup>

Polycrystalline magnesium silicide,  $\text{Mg}_2\text{Si}$  and magnesium germanide,  $\text{Mg}_2\text{Ge}$  were synthesised from the elemental powders via the microwave-induced-metal-plasma (MIMP) approach at 200 W within 1 min *in vacuo* for the first time. The formation of reactive Mg plasma facilitated by the high-frequency electromagnetic field (2.45 GHz) is at the origin of the ultrafast reaction kinetics in these preparations. Powder X-ray diffraction (PXRD), Scanning Electron Microscopy (SEM) combined with Energy Dispersive X-ray Spectroscopy (EDX) and X-ray Photoelectron Spectroscopy (XPS) attest to the high purity of the products. Both SEM and Transmission Electron Microscopy (with Selected Area Electron Diffraction) (TEM/SAED) demonstrate the pseudomorphic nature of the metal plasma reactions such that use of nanoporous Ge starting material leads to the production of nanoporous germanide,  $\text{Mg}_2\text{Ge}$ . Covalent Mg–Si and Mg–Ge bonds with partial ionic character are suggested by XPS, while the refined crystal structures are consistent with Mg–Mg interactions within the cubane-like clusters in  $\text{Mg}_2\text{X}$  antifluorite unit cells. The MIMP method unlocks not only the sustainable synthesis of  $\text{Mg}_2\text{X}$  materials but also the wider production of intermetallics and *Zintl* phases of prescribed morphology.

Received 24th May 2022,  
Accepted 22nd July 2022

DOI: 10.1039/d2ce00721e

rsc.li/crystengcomm

## Introduction

The societal benefits of a low-carbon future demand the means of harvesting, producing, converting and storing renewable energy efficiently. Energy demand and utilisation must also be efficiently managed. The sustainable green synthesis and fabrication of functional solid-state materials and devices is an integral part of this process; energy consumption and environmental impact must be minimised as a priority.<sup>1–3</sup> For several decades now, the physics of microwaves (MWs) has inspired the creativity of synthetic chemists.<sup>4,5</sup> Correspondingly, MW synthesis routes have produced a myriad of inorganic solid materials with various structures and morphologies. Simultaneously, the major benefits of time/energy savings; rapid heating rates; fast

throughput; precise, selective heating, and reduction of waste heat/hazardous chemicals have been delivered.<sup>2–11</sup> Nevertheless, MW synthesis still faces many challenges before its implementation as a primary route to advanced materials manufacturing could be considered.<sup>2–7,10</sup>

The  $\text{Mg}_2\text{X}$  (X = Si, Ge, Sn) family crystallises with the face-centered cubic, antifluorite structure (space group  $Fm\bar{3}m$ ) in which Mg atoms occupy the 8c (1/4, 1/4, 1/4) interstitial sites within a CCP lattice of X atoms (4a sites; Fig. 1b).<sup>5,12</sup> These *Zintl* phase compounds are intrinsically n-type semiconductors with narrow indirect band gaps (*e.g.* *ca.* 0.73, 0.72 and 0.31 eV experimentally for  $\text{Mg}_2\text{Si}$ ,  $\text{Mg}_2\text{Ge}$  and  $\text{Mg}_2\text{Sn}$ , respectively).<sup>13,14</sup> Since the 1960s, members of the  $\text{Mg}_2\text{X}$  family (often forming solid-solutions) have continuously emerged as promising energy materials given excellent mid-temperature (*ca.* 500–800 K) thermoelectric (TE) performance combined with simple structures and flexible compositions of abundant, non-toxic environmentally-friendly elements.<sup>5,12</sup> Common traits of large Seebeck coefficients, high electrical conductivity and unusually low lattice thermal conductivities permit the dimensionless figure of merit (*zT*) values to exceed unity comfortably for n-type  $\text{Mg}_2\text{X}$  materials.<sup>15–18</sup> More recently,  $\text{Mg}_2\text{X}$  compounds have been proposed as candidate anode materials for rechargeable Mg-ion batteries,<sup>19–21</sup> and these  $\text{Mg}_2\text{X}$  materials (especially  $\text{Mg}_2\text{-Si}$ ) have also demonstrated promise as the basis for the large-scale fabrication of nanoporous X anodes for Li- and Na-ion

<sup>a</sup> WestCHEM, School of Chemistry, University of Glasgow, Joseph Black Building, Glasgow, G12 8QQ, UK. E-mail: Duncan.Gregory@glasgow.ac.uk; Tel: +44 (0)141 330 8128

<sup>b</sup> Department of Chemical Engineering, R&D Center for Membrane Technology, Research Center for Circular Economy, Chung Yuan Christian University, 32023, No. 200, Chun Pei Rd., Chung Li District, Taoyuan City 32023, Taiwan

<sup>c</sup> Faculty of Chemistry, Nicolaus Copernicus University in Toruń, ul. Gagarina 7, 87-100 Toruń, Poland

<sup>†</sup> Electronic supplementary information (ESI) available. See DOI: <https://doi.org/10.1039/d2ce00721e>



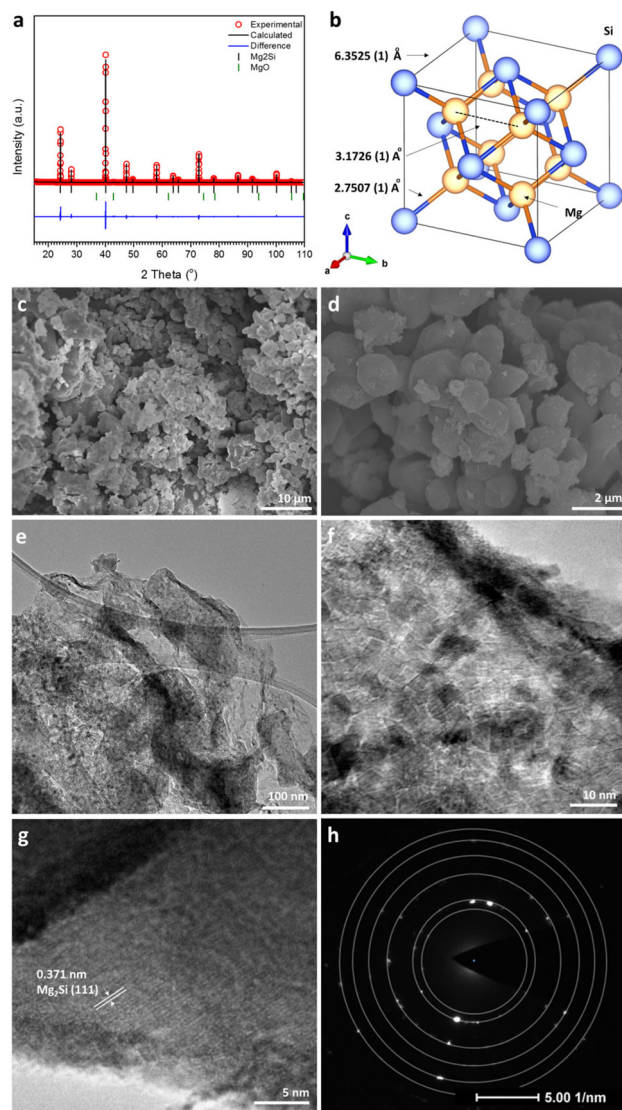


**Fig. 1** Results from PXRD and electron microscopy for the MIMP-synthesised  $\text{Mg}_2\text{Si}$  powders, showing (a and b) profile plot of the Rietveld refinement against PXD data and the corresponding crystal structure; (c and d) SEM images, (e–g) TEM images, and (h) SAED pattern taken from the area shown by the image in (g).

secondary batteries.<sup>5,22–26</sup> Beside applications in energy conversion and storage, narrow-gap  $\text{Mg}_2\text{X}$  compounds are considered as good candidates for infrared optoelectronic devices,<sup>27</sup> whereas the mechanical and anti-corrosive properties of  $\text{Mg}_2\text{Si}$  prove it an effective additive in metallurgy and for biodegradable implants.<sup>28–30</sup> Presciently, the high-profile medical value of non-toxic  $\text{Mg}_2\text{Si}$  nanoparticles as an outstanding deoxygenation agent for cancer starvation therapy has been discovered recently.<sup>31</sup>

Among several well-established synthesis routes to  $\text{Mg}_2\text{X}$  materials, conventional high-temperature solid-state methods and reactive ball-milling synthesis typically require long durations, whereas newer spark plasma sintering (SPS) and self-propagating high-temperature synthesis methods still require high temperatures and special equipment

requirements.<sup>5,12,15–17,20</sup> Careful and/or multiple-step treatments are often needed. These synthesis approaches have to compromise the different physical and chemical properties of reactants and products, such as the solubility of Mg cations in solid-state X phases, boiling/melting points, volatility of Mg, mechanical hardness or ductility, and the ready tendency of Mg (and its products) to oxidise in air.<sup>5,12,15–17,32,33</sup> Accordingly, the compositions of final products can be challenging to control, often involving impurities and potential safety issues (e.g. air exposure may cause the self-ignition of ball-milled products).<sup>5,17,20,32</sup> A few early attempts to synthesise  $\text{Mg}_2\text{Si}$ -based TE materials in the solid state using MWs demanded very high input powers (a few KW) for tens of minutes under inert conditions.<sup>5,34,35</sup> It was the pioneering work of Savary *et al.* in 2010 that first led to the successful production of  $\text{Mg}_2\text{Si}$  nanopowders, placing an encouraging milestone for the MW synthesis of  $\text{Mg}_2\text{X}$  compounds (although control of purity could not then be mastered).<sup>36</sup> In this case, pucks of Mg and Si powders were ball-milled for 2 h prior to heating using an incident MW power of only 175 W for 2 min under  $\text{N}_2$ .<sup>36</sup> Savary *et al.* applicator possessed the capability to deliver two modes of MW excitation separately to the sample; both magnetic and electric field components. Their experimental observations indicated that semiconducting Si coupled with the magnetic field whereas Mg coupled to neither mode and that it was the rapid heating of Si that principally drove the reaction towards  $\text{Mg}_2\text{Si}$ .<sup>5,36</sup> A similar instrument and methodology were then applied to prepare both n- and p-doped  $\text{Mg}_2\text{Si}$ .<sup>37</sup> This was perhaps unexpected given that both theory and experiment demonstrate that fine metal powders can couple with MWs (at 2.45 GHz) to reach high temperatures rapidly.<sup>2–5,10</sup>

We previously conceived a new microwave-induced-metal-plasma (MIMP) approach towards the synthesis of phase-pure  $\text{Mg}_2\text{Sn}$  within 1 min, employing an incident power of 200 W *in vacuo*.<sup>3,5</sup> In (sub)micron form, Mg and Sn powders coupled effectively with the MW field to form reactant metal plasmas (composed of ionised cations and electrons) *in situ*, such that the reaction kinetics were significantly promoted in the presence of the 2.45 GHz electromagnetic field.<sup>3,5</sup> This new approach, where synthesis occurs *via* the reaction of species in the plasma phase, contrasts markedly with high-temperature solid-state reactions. The diffusion of atoms/ions in the *solid state* is relatively slow even at elevated temperatures and at the increased heating rates achievable by MW heating. Herein, we extend the MIMP method to the reaction of Mg with the metalloids Si and Ge in the rapid, energy-efficient synthesis of crystalline  $\text{Mg}_2\text{Si}$  and  $\text{Mg}_2\text{Ge}$ . Notably, the MIMP reaction between Mg and nanoporous Ge preserved the nanostructure of the latter in the  $\text{Mg}_2\text{Ge}$  product, affirming that Mg plasma is the key reactive species in the  $\text{Mg}_2\text{X}$  syntheses. In these respects, the MIMP method contrasts distinctively with MW syntheses in the solid state,<sup>36,37</sup> showing great promise for Mg-based phases and for other alloys and compounds more broadly.



## Experimental

### Materials synthesis

The syntheses of  $\text{Mg}_2\text{Si}$  and  $\text{Mg}_2\text{Ge}$  followed similar procedures to that of  $\text{Mg}_2\text{Sn}$  in our previous study.<sup>3,5</sup> All manipulations and preparations were performed inside an  $\text{N}_2$ -filled LABstar glovebox (mBraun;  $\text{H}_2\text{O}$ ,  $\text{O}_2 < 0.5$  ppm). Typically, either 70 mg (2.88 mmol) of Mg (99.8%, 325 mesh, Alfa Aesar) was combined with 35 mg (1.25 mmol) of Si (99.5%, 325 mesh, Sigma Aldrich) or 35 mg (1.44 mmol) of Mg (99.8%, 325 mesh, Alfa Aesar) with 45 mg (0.62 mmol) of nanoporous Ge (synthesised from  $\text{Mg}_2\text{Ge}$  by de-alloying using literature methods<sup>38</sup>) and mixed thoroughly before the transfer of the respective powders into an alumina crucible (which can be considered MW-transparent). One control experiment using 35 mg of Mg and 45 mg of commercial bulk Ge powders (Trace metal basis, 99.999%, Acros Organics) was also performed (full details in ESI†). In each case, an excess of Mg powder (15 at%) was employed (equating to a 2.3:1 molar ratio) to compensate for the evaporation of Mg.<sup>3,5</sup> The crucible was placed within a quartz tube, which was subsequently closed and connected to a vacuum line outside the glovebox.

A modified single-mode cavity MW reactor (CEM Discovery, 2.45 GHz) with the input power adjustable from 0–300 W was employed.<sup>3,5</sup> An incident MW power of 200 W was applied to the powder mixture under a static vacuum of  $P < 10^{-6}$  mbar.<sup>5</sup> The irradiation time was typically 60 s for both  $\text{Mg}_2\text{Si}$  and  $\text{Mg}_2\text{Ge}$ . In order to analyse the composition during the reaction, one  $\text{Mg}_2\text{Ge}$  experiment was performed for 30 s. Following the irradiation, the quartz tube was allowed to cool naturally to room temperature. All samples were ground and stored in the glovebox for further characterisation.

### Materials characterisation

Powder X-ray diffraction (PXRD) was performed using a PANalytical X'pert Pro MPD diffractometer in Bragg–Brentano geometry ( $\text{Cu-K}\alpha_1$ ,  $\lambda = 1.5406$  Å; accelerating voltage of 40 kV; emission current of 40 mA). For phase identification purposes, PXRD patterns were collected at room temperature over a  $2\theta$  range of 15–85° with a step size of 0.0334° and 30 s per step. For structure determination/quantitative analysis by Rietveld refinement, PXRD datasets were collected over extended ranges of 15–110° and 15–100° ( $2\theta$ ) for  $\text{Mg}_2\text{Si}$  and  $\text{Mg}_2\text{Ge}$  respectively, with a step size of 0.01667° and 100 s per step. Previously published  $\text{Mg}_2\text{Si}$ ,  $\text{Mg}_2\text{Ge}$ , Si, Ge, MgO and Mg structures were used for phase identification purposes and as initial models for Rietveld refinements.<sup>39–44</sup> Rietveld refinements were performed by using GSAS *via* the EXPGUI interface.<sup>45</sup> As-refined crystal structures were plotted using the VESTA package.<sup>46</sup>

Scanning Electron Microscopy (SEM) and Energy Dispersive X-ray Spectroscopy (EDX) were performed using a Philips/FEI XL30 ESEM instrument (beam voltage 20 kV, maximum magnification 20 k) equipped with an INCA X-Act

detector (Oxford Instruments Analytical, UK). The samples were coated with Pt plasma under vacuum to optimise the quality of SEM images. Transmission Electron Microscopy (TEM) and selected area electron diffraction (SAED) were performed using an FEI Tecnai G2 F20 X-Twin; 200 kV, FEG microscope. High-resolution Si2p, Ge3d, and Mg1s X-ray Photoelectron Spectroscopy (XPS) spectra were measured using a monochromatic Al-K $\alpha$  Photoelectron Spectrometer (Thermo Scientific) under vacuum, both before and after etching with an Ar-ion beam (at 2.0 keV for 30 s).

## Results and discussion

### MIMP synthesis and characterisation of $\text{Mg}_2\text{Si}$

MW syntheses of  $\text{Mg}_2\text{Si}$  and  $\text{Mg}_2\text{Ge}$  were conducted from elemental mixtures with an initial Mg/Si or Mg/Ge ratio of 2.3:1, under a static vacuum of  $P < 10^{-6}$  mbar with an incident power of 200 W, typically for a duration of 60 s. Plasma formed almost immediately (within *ca.* 2 s of MW irradiation), evolving initially from a pale purple colour to persistent green for both samples. These closely resembled the plasmas observed in the MIMP synthesis of  $\text{Mg}_2\text{Sn}$ ,<sup>5</sup> suggesting the dominance of Mg plasma formation across the MIMP syntheses of the wider  $\text{Mg}_2\text{X}$  family ( $\text{X} = \text{Sn}$ , Si, Ge).<sup>3,5</sup> Fine dark blue powders were obtained from the reaction in each case, with no visible evidence of sintering or agglomeration to larger solid pieces.

Fig. 1a shows the profile plot obtained from the Rietveld refinement performed against laboratory PXRD data for the  $\text{Mg}_2\text{Si}$  product synthesised from 60 s of irradiation. The silicide formed with the cubic antiferroite structure (space group  $Fm\bar{3}m$ ) with a lattice parameter of  $a = 6.3525(1)$  Å (Fig. 1b; Table 1), in good agreement with previous reports in the literature.<sup>39</sup> The refinement indicated that the sample was Mg-deficient with a site-occupancy-factor (SOF) of 0.976(4) for the Mg site (Table 2). Mg sub-stoichiometry and vacancies on the Mg site are not uncommon features in  $\text{Mg}_2\text{-Si}$  synthesized at high temperature (and/or reduced pressure) and occur even in the presence of excess magnesium due to a combination of evaporation and oxidation (to MgO).<sup>17,47,48</sup>

**Table 1** Crystallographic data from the Rietveld refinement of MIMP-synthesised  $\text{Mg}_2\text{Si}$  (irradiated for 60 s)

Chemical formula	$\text{Mg}_2\text{Si}$	MgO
Crystal system	Cubic	Cubic
Space group	$Fm\bar{3}m$ (no. 225)	$Fm\bar{3}m$ (no. 225)
Lattice parameter, $a/\text{\AA}$	6.3525(1)	4.2176(3)
Cell volume/ $\text{\AA}^3$	256.346(9)	75.024(17)
Formula weight/ $\text{g mol}^{-1}$	302.032	161.216
Formula units, $Z$	4	4
Calculated density/ $\text{g cm}^{-3}$	1.956	3.568
Phase fraction/wt%	98.9(6)	1.1(6)
No. of variables	35	
No. of observations	5628	
$wR_p$	0.1576	
$R_p$	0.1194	
$\chi^2$	5.611	





**Table 2** Atomic parameters for MIMP-synthesised  $\text{Mg}_2\text{Si}$  (irradiated for 60 s)

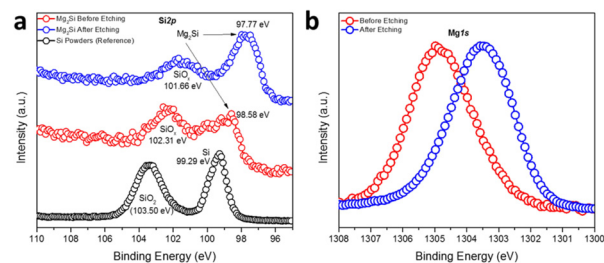
Atom	Site	<i>x</i>	<i>y</i>	<i>z</i>	$100 \times U_{\text{iso}}/\text{\AA}^2$	SOF
Mg	8c	0.25	0.25	0.25	2.85(4)	0.976(4)
Si	4a	0	0	0	2.74(5)	1

Interestingly, such Mg vacancies rarely lead to intrinsic p-doping due to the trapping of states within the band gap. Nevertheless, the PXRD results showed that the MIMP method yields crystalline  $\text{Mg}_2\text{Si}$  of high purity (98.9(6) wt%), with the almost negligible amount of MgO (1.1(6) wt%) likely originating from the surface oxidation of  $\text{Mg}_2\text{Si}$  during handling and the reaction of Mg plasma with trace amounts of oxygen in the closed quartz tube (Table 1).<sup>5,17,31</sup>

The SEM images show highly crystalline fine powders with a relatively uniform size distribution ranging from sub-microns to  $\sim 1 \mu\text{m}$  across (Fig. 1c and d). In addition to this majority of particles, small clusters of much smaller (nanoscale) particles can be observed, which were potentially formed by the rapid reaction of Mg plasma with pulverised or existing Si nanoparticles and with the small amount of residual oxygen in the tube. Additional pulverisation of  $\text{Mg}_2\text{Si}$  itself is also perhaps not surprising given the action of the plasma on the particles in the MW field. The observation of the nanoparticles herein is consistent with findings from our previous MIMP study on  $\text{Mg}_2\text{Sn}$ .<sup>5</sup> The EDX spectrum corresponding to the section of sample imaged in Fig. 1d led to an Mg/Si atomic ratio of  $2.0 \pm 0.1$ , in excellent agreement with the theoretical composition of  $\text{Mg}_2\text{Si}$  (Fig. S1a, ESI†). The presence of a small concentration of O at the sample surface might be attributed largely to the brief air exposure during specimen transfer. The maps of Mg and Si confirm the uniform distribution of the elements across the surface of the MIMP-synthesised powder (Fig. S1b and c, ESI†).

The low-magnification TEM images in Fig. 1e showed that typical micron/sub-micron  $\text{Mg}_2\text{Si}$  particles were rich in grain boundaries. At higher magnification (Fig. 1f), it was evident that the  $\text{Mg}_2\text{Si}$  particles were composed of a multitude of crystalline nanograins, each *ca.* 5–10 nm across. On closer inspection (Fig. 1g), TEM images provided evidence of: (i) a disordered surface layer of *ca.* 1–2 nm in thickness, which potentially stemmed from a surface reaction when exposed to oxygen/water in air. This is consistent with the reactivity of  $\text{Mg}_2\text{Si}$ , especially in powder form, and the formation of a passivation layer<sup>31</sup> and (ii) highly crystalline regions beneath the surface layer, where lattice fringe spacings of 0.371 nm predominated, matching well with the (111) planes in  $\text{Mg}_2\text{Si}$  (and consistent with PXRD results; Fig. 1a).<sup>39</sup> Fig. 1h shows a typical SAED pattern from the sample and as taken from the region shown in Fig. 1g. The pattern is typical of a polycrystalline material, with diffraction rings that can be indexed to  $\text{Mg}_2\text{Si}$ . These data affirm that the crystalline material is bulk  $\text{Mg}_2\text{Si}$  encapsulated with a thin layer of oxide that likely forms instantaneously when handled in air (Table S1, ESI†).

The oxidation states and binding energies of Mg and Si in the  $\text{Mg}_2\text{Si}$  *Zintl* phase were further investigated by measuring high-resolution Si2p and Mg1s XPS spectra (Fig. 2). Compared to a reference spectrum taken for Si powder, which also featured distinct peaks for  $\text{SiO}_2$  in addition to those for Si(0), the spectrum from a sample of as-synthesised  $\text{Mg}_2\text{Si}$  powder showed the co-existence of two broad peaks covering binding energies corresponding to  $\text{SiO}_2$  ( $\text{SiO}_x$ ), Si(0) and Si species that appeared more anionic in character as would befit  $\text{Mg}_2\text{Si}$  (at 98.58 eV) (Fig. 2a).<sup>49,50</sup> Impurity peaks might be expected from the surface oxidation of  $\text{Mg}_2\text{Si}$  in air (just as the Si reference sample was surface-oxidised). The sample was subsequently etched with an Ar-ion beam and although the treatment could not completely remove all the oxidised surface species, the predominant Si peak was identified at a binding energy of 97.77 eV, which is significantly lower than that expected for elemental Si (99.29 eV), revealing the nominally negative oxidation state of Si in  $\text{Mg}_2\text{Si}$  (Fig. 2a).<sup>49,50</sup> One peak was discovered in the Mg1s XPS spectrum (Fig. 2b) and this shifted to lower binding energy post-etching. The initial observation suggests the presence of a passivating surface layer of MgO, as could be inferred from electron microscopy. Post etching, however, the Mg peak is located at a binding energy intermediate between MgO (1304.5 eV) and Mg (1303.0 eV), suggesting an oxidation state of Mg between formally +2, as in MgO, and of 0 in Mg metal.<sup>51</sup> The XPS data indicated that the bonding in  $\text{Mg}_2\text{Si}$  was by no means purely ionic (*i.e.* in which Mg valence electrons were entirely transferred to Si) but possessed significant covalent character.<sup>13,14,52,53</sup> The spectra and inferences are entirely consistent with comprehensive studies of (oxidised)  $\text{Mg}_2\text{Si}$  on Si (111) made more than 2 decades ago.<sup>54</sup> Interestingly, the refined Mg–Mg distance in  $\text{Mg}_2\text{Si}$  was only 3.1726(1) Å, which is rather shorter than the equivalent distance in Mg metal (3.1967(4) Å). This presents the possibility of “free” electrons within the cubic  $\text{Mg}_8$  sublattice in Fig. 1b.<sup>40,52</sup> Our XPS and PXRD results concur with previous studies on  $\text{Mg}_2\text{Si}$  when a charge transfer from Mg to Si was calculated as 0.16 units by applying a potential model to XPS data; this corresponds to an Mg–Si bond with an ionicity of 8%.<sup>50,55</sup> Subsequent Bader charge analysis implied that Mg carries a charge of +1.45 and Si could be attributed a charge of –2.90.<sup>52</sup> The vacant cavity at the body centre of the unit cell is proposed to form a concentration of electron

**Fig. 2** High-resolution (a) Si2p and (b) Mg1s XPS spectra of MIMP-synthesised  $\text{Mg}_2\text{Si}$  powders (irradiated for 60 s).

density originating from the overlapping Mg 3p states, which in turn are primarily responsible for the conduction band minimum (CBM) (at the X point in the Brillouin zone) in the electronic structure of Mg<sub>2</sub>Si. This is a point that we will return to when discussing the Mg<sub>2</sub>X phases below.

### MIMP synthesis and characterisation of Mg<sub>2</sub>Ge

The MW exposure of Mg and Ge powders to an incident MW power of 200 W for 30 s was able to generate a product dominated by Mg<sub>2</sub>Ge (94.3(3) wt%). The remainder of the sample was composed of a small amount of unreacted starting materials (Mg: 4.1(3) wt% and Ge: 1.5(1) wt%), as indicated by the Rietveld refinement profile shown in Fig. 3a (see also ESI† Tables S2 and S3). PXRD confirmed that irradiation of the elements at 200 W for double the duration (60 s) led to their complete reaction, with one very weak diffraction peak at 42.8° 2θ suggesting the presence of MgO.<sup>44</sup> Correspondingly, the Rietveld refinement revealed a phase purity of 98.1(1) wt% for Mg<sub>2</sub>Ge with the remainder of the sample corresponding to MgO (1.9(1) wt%) (Fig. 3b; Table 3). As with the Mg<sub>2</sub>Si sample, the presence of MgO as a minor phase could originate from handling during sample transfer and measurement, with the additional caveat that the nanoporous Ge reactant is quite likely to also react with air to oxidise at its surface, presenting a potential source of oxygen at the outset.<sup>17</sup> The Rietveld refinement confirmed Mg<sub>2</sub>Ge to be isostructural with Mg<sub>2</sub>Si, with a lattice parameter of  $a = 6.3940(1)$  Å and an Mg–Mg distance of 3.1970(1) Å, equivalent to that in Mg metal (3.1967(4) Å) within 1σ.<sup>40</sup> In contrast to Mg<sub>2</sub>Si, we found no evidence of non-stoichiometry at the Mg 8c site; attempts to refine the SOF led to no significant departure from unity and did not improve the overall fit to the profile or the *R* factors (Table 4).

Fig. 4a and b show SEM images taken for the Mg<sub>2</sub>Ge powder synthesised at 200 W for 60 s. For comparison, the size and morphology of the nanoporous Ge reactant powder are indicated in the SEM images in the ESI† (Fig. S2). The Mg<sub>2</sub>Ge powders take the appearance of individual micron-sized particles, which can be viewed as pieces of a nanoporous “bulk” matrix composed of nano ligaments

**Table 3** Crystallographic data from the Rietveld refinement of MIMP-synthesised Mg<sub>2</sub>Ge (irradiated for 60 s)

Chemical formula	Mg <sub>2</sub> Ge	MgO
Crystal system	Cubic	Cubic
Space group	<i>Fm</i> 3 <i>m</i> (no. 225)	<i>Fm</i> 3 <i>m</i> (no. 225)
Lattice parameter, <i>a</i> /Å	6.3940(1)	4.2236(4)
Cell volume/Å <sup>3</sup>	261.403(6)	75.344(22)
Formula weight/g mol <sup>−1</sup>	484.800	161.216
Formula units, <i>Z</i>	4	4
Calculated density/g cm <sup>−3</sup>	3.080	3.553
Phase fraction/wt%	98.1(1)	1.9(1)
No. of variables	34	
No. of observations	5085	
<i>wR</i> <sub>p</sub>	0.1626	
<i>R</i> <sub>p</sub>	0.1190	
$\chi^2$	2.382	

ranging from *ca.* 85–300 nm across. An appraisal of the SEM images from both the nanoporous Ge reactant powder and the nanoporous Mg<sub>2</sub>Ge product demonstrates the close resemblance of the former and latter. This similarity signals the pseudomorphic nature of the MIMP reaction. In many ways, this is not an unreasonable result. For example, there are many examples of nanoporous matrices of p-block metals/metalloids possessing the capability for Li<sup>+</sup>, Na<sup>+</sup> or Mg<sup>2+</sup> ion insertion during electrochemical alloying reactions in rechargeable-ion batteries; such processes can have minimal effects on the nanostructure, extending cyclability over equivalent bulk materials.<sup>22–26</sup> One can also further infer from this result that the MIMP process, at least in the case of Mg<sub>2</sub>Ge, is one that involves a solid-plasma phase reaction between Ge and Mg respectively, reinforcing the hypothesis made above concerning the MW reaction mechanism in the Mg–Si system.<sup>3,5</sup> This premise was reinforced by conducting a supplementary MIMP synthesis of Mg<sub>2</sub>Ge from a mixture of Mg and commercial, bulk Ge powers (99.999%, Acros Organics). Revealingly, this experiment led to the production of non-porous, micron-sized Mg<sub>2</sub>Ge particles (ESI† Fig. S3).

Fig. 4c shows a representative EDX spectrum, yielding an atomic Mg:Ge:O ratio of 60.39:23.81:15.80. Fig. 4d–f show that elemental distributions of Mg, Ge and O were uniform across the surface of the specimen, demonstrating the homogeneity of the MIMP-synthesised product. In light of the known reactivity of Mg<sub>2</sub>Ge with water,<sup>5,31,56</sup> the EDX data suggest that a surface passivation occurs following exposure to air as the sample was transferred to the SEM chamber:

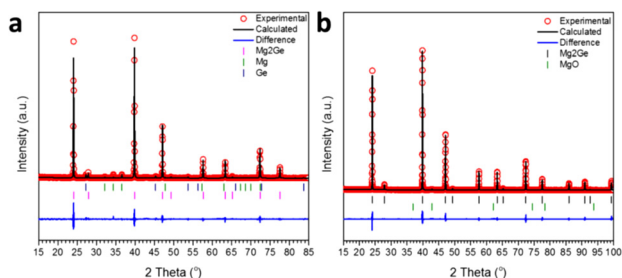


**Fig. 3** Profile plot of the Rietveld refinements against PXRD data for Mg<sub>2</sub>Ge samples synthesised at 200 W with a MW irradiation time of: (a) 30 s and (b) 60 s, respectively.

**Table 4** Atomic parameters for MIMP-synthesised Mg<sub>2</sub>Ge (irradiated for 60 s)

Atom	Site	<i>x</i>	<i>y</i>	<i>z</i>	100 × <i>U</i> <sub>iso</sub> /Å <sup>2</sup>	SOF
Mg	8c	0.25	0.25	0.25	2.52(6)	1
Ge	4a	0	0	0	2.10(4)	1



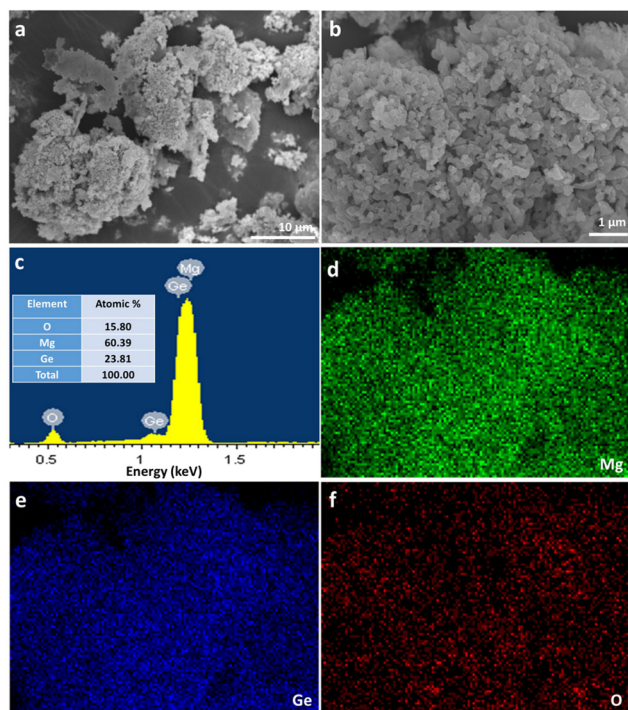


Fig. 4 SEM characterisation of  $\text{Mg}_2\text{Ge}$  powders synthesised from Mg and Ge at 200 W with an irradiation time of 60 s, showing: (a and b) SEM images at different magnification; (c) a representative EDX spectrum taken from the area shown in the image in (b); and (d–f) elemental maps of Mg, Ge and O, respectively, taken from the same area shown in (b).

Indeed, we tested the reactivity of samples of  $\text{Mg}_2\text{X}$  ( $\text{X} = \text{Si}$ , Ge and Sn) with deionised water (*ca.* 100 mL in a beaker;  $\text{Mg}_2\text{Sn}$  was prepared as per ref. 5).  $\text{Mg}_2\text{Ge}$  reacted rapidly with water, generating a white precipitate within a few seconds.  $\text{Mg}_2\text{Si}$  reacted with water less vigorously, forming a white precipitate over the course of several minutes. By comparison, the reaction of  $\text{Mg}_2\text{Sn}$  was slow (*i.e.* reaction continued to occur after 24 h), forming a dense grey/white powder. Moreover, reactions of  $\text{Mg}_2\text{Si}$  and  $\text{Mg}_2\text{Ge}$  with 0.1 M HCl aqueous solutions formed gaseous bubbles which could be ignited in air, assumed to be  $\text{SiH}_4$  and  $\text{GeH}_4$  gases, respectively, in accord with previous observations for  $\text{Mg}_2\text{Si}$  and  $\text{Mg}_2\text{Ge}$ .<sup>31,56</sup>

The surface composition and the oxidation states of Mg and Ge in  $\text{Mg}_2\text{Ge}$  were further investigated by the measurement of high-resolution Ge3d and Mg1s XPS spectra (Fig. 5). Spectra confirmed the presence of the oxide passivation layer suggested by SEM/EDX results. The Ge3d XPS spectra (Fig. 5a) showed that Ar-ion beam etching can effectively remove this surface oxide layer (which likely formed during the transfer of the XPS specimen to the vacuum chamber). The experimental spectra for  $\text{Mg}_2\text{Ge}$  were compared to those from a reference of Ge powder. Prior to Ar-etching, the Ge3d spectra for  $\text{Mg}_2\text{Ge}$  showed little evidence for Ge(0) and only a relatively small peak corresponding to a binding energy typical for  $\text{GeO}_2$  (at 32.21 eV). This peak was effectively removed from the spectrum post-etching. As

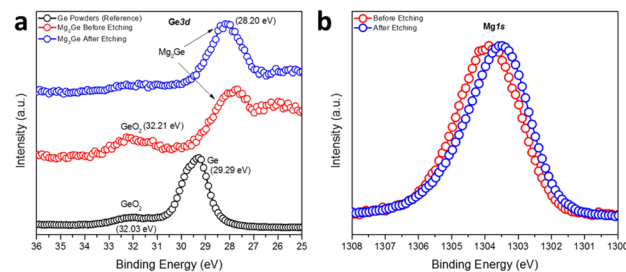


Fig. 5 High-resolution (a) Ge3d and (b) Mg1s XPS spectra of the MIMP-synthesised  $\text{Mg}_2\text{Ge}$  powders with an irradiation time of 60 s.

witnessed for Si in the equivalent Si2p XPS spectra taken for  $\text{Mg}_2\text{Si}$ , the main Ge peak shifts significantly to lower binding energy as compared to that in the elemental spectrum (of Ge(0)). The shift of >1 eV (from 29.29 eV to 28.2 eV) indicates a nominal negative oxidation state for Ge in  $\text{Mg}_2\text{Ge}$ .<sup>57</sup> The Mg1s spectrum is rather similar to that seen for  $\text{Mg}_2\text{Si}$ . Fig. 5b shows that, post-etching, the Mg1s peak is centred at *ca.* 1303.5 eV, which is located between the binding energies expected for MgO (1304.5 eV) and Mg (1303.0 eV), suggesting an oxidation state of Mg between +2 in MgO and 0 in Mg metal.<sup>51–53</sup> In similarity to  $\text{Mg}_2\text{Si}$ , therefore, XPS reveals that the bonding in the germanide is likely to be predominantly covalent.

### Trends in the structures of MIMP-synthesised $\text{Mg}_2\text{X}$ ( $\text{X} = \text{Si}$ , Ge, Sn) and common features of the MIMP syntheses

Selected structural data for the  $\text{Mg}_2\text{X}$  ( $\text{X} = \text{Si}$ , Ge, Sn) antifluorite compounds, as determined from Rietveld refinement, are presented in Fig. 6. As would be expected,  $\text{Mg}_2\text{Sn}$  has a larger cubic lattice parameter ( $a = 6.7653(1)$  Å), Mg–X bond length (2.9295(1) Å) and Mg–Mg distance (3.3827(1) Å) when compared to  $\text{Mg}_2\text{Si}$  and  $\text{Mg}_2\text{Ge}$ .<sup>5</sup>  $\text{Mg}_2\text{Ge}$  exhibits a very similar cubic lattice parameter to  $\text{Mg}_2\text{Si}$ , reflecting the rather similar covalent radii of the elements. Consequently, and given that both Mg and X are located on

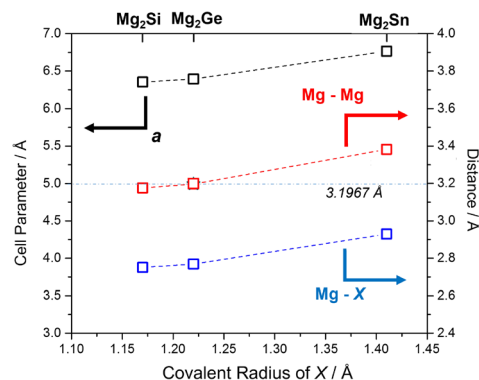
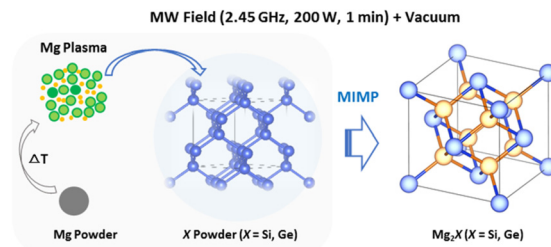


Fig. 6 Plot of refined lattice parameter,  $a$  (black), Mg–X (blue) and Mg–Mg (red) distances<sup>5</sup> for MIMP-synthesised  $\text{Mg}_2\text{X}$  ( $\text{X} = \text{Si}$ , Ge, Sn) (200 W, 1 min) against covalent radius of X.<sup>60</sup> The horizontal line and value represents the Mg–Mg distance in Mg metal.<sup>40</sup>



special positions (of  $(1/4, 1/4, 1/4)$  and  $(0,0,0)$ , respectively), the Mg–X ( $X = \text{Si, Ge}$ ) bond lengths and Mg–Mg distances vary by only *ca.* 0.02 Å. It should also be noted that the Mg–Mg distances (within the cubane-like  $\text{Mg}_8$  cluster) is only 3.1762(1) and 3.1970(1) Å for  $\text{Mg}_2\text{Si}$  and  $\text{Mg}_2\text{Ge}$ , respectively and therefore equal or less than the Mg–Mg distance in Mg metal (3.1967(4) Å).<sup>40,52,58</sup> This implies potential metal–metal interactions and the presence of “free” electrons within the central cavity of the cubic  $\text{Mg}_8$  sub-lattice in both  $\text{Mg}_2\text{Si}$  and  $\text{Mg}_2\text{Ge}$ . The recent computational study that identified such electrons as being associated with the CBM (through both  $\sigma$  and  $\pi$  bonding Mg 3p<sub>y</sub> states interacting with Si 3d states) suggested that these cavity electrons are likely mobile and associated with the intrinsic n-type semiconductivity of  $\text{Mg}_2\text{Si}$  (and, in fact, these cavity states are deep lying enough to resemble those in inorganic electrides).<sup>52</sup> The structural data would suggest that  $\text{Mg}_2\text{Ge}$  is likely to behave in a similar way and that the transport properties of both compounds could be tuned by modifying the size of the central cavity. Interestingly, single crystal X-ray structural studies had previously suggested that  $\text{Mg}_2\text{Si}$  could accommodate additional interstitial Mg in the vacant body centre  $(1/2, 1/2, 1/2)$  position, albeit at very low levels ( $<1\%$ ).<sup>59</sup> Simultaneously, there was a tendency for the crystals to exhibit Mg vacancies of up to 1% at the 8c  $(1/4, 1/4, 1/4)$  position and that as these vacancies increased so the electrical conductivity decreased (and the Seebeck coefficient increased). Our structural data suggest Mg vacancy levels of *ca.* 2% at the 8c site in  $\text{Mg}_2\text{Si}$ , but lab PXRD could not resolve the presence of electron density at the 1–2% level at the body centre. The presence of analogous vacancies in MIMP-synthesised  $\text{Mg}_2\text{Ge}$  and  $\text{Mg}_2\text{Sn}$ <sup>5</sup> could not be so readily established. There is clearly a need for a still more comprehensive understanding of the links between structure, composition and electronic properties in  $\text{Mg}_2\text{Si}$  and to explore to what extent these are replicated or otherwise in other  $\text{Mg}_2\text{X}$  Zintl phases. The links between “cation” vacancies and the presence of either interstitial Mg or electrons could also have profound implications for ionic transport and the application of  $\text{Mg}_2\text{X}$  as anodes in Mg-ion batteries.<sup>19–21</sup>

The observed plasma generation during our MIMP syntheses of  $\text{Mg}_2\text{X}$  ( $X = \text{Si, Ge}$ ) and for  $\text{Mg}_2\text{Sn}$ <sup>5</sup> was very similar, *i.e.* a transition from an initial purple coloured plasma (within *ca.* 10 s) to a steady green plasma. This is despite the very different physical and chemical properties of Sn, Si and Ge as reactants, where semiconducting Si and Ge have much higher melting points and hardness factors, for example, than metallic Sn.<sup>5,17</sup> Given the volatility of Mg, it is not altogether surprising that Mg plasma formation is pivotal in the synthesis of  $\text{Mg}_2\text{X}$  ( $X = \text{Si, Ge, Sn}$ ) Zintl phases in a microwave field under vacuum.<sup>3,5</sup> The pseudomorphic reaction of Mg with nanoporous Ge underlines the premise that Mg is in the plasma state during each of these MW syntheses. Given that plasma is essentially a gas formed from ions and electrons, the  $\text{Mg}_2\text{Si}$  and  $\text{Mg}_2\text{Ge}$  synthesis processes can be likened to many conventional high temperature solid–



**Scheme 1** Schematic of the principal Mg plasma-enabled reaction route proposed for the MIMP synthesis of  $\text{Mg}_2\text{Si}$  and  $\text{Mg}_2\text{Ge}$ .

gas reactions, which are often similarly pseudomorphic.<sup>61,62</sup> The principal difference in the MIMP case is that it is the *metal* starting material that reacts ostensibly in the gaseous phase. Any contrast, therefore, between the MIMP  $\text{Mg}_2\text{X}$  reactions mainly lies in the state of X. For Si and Ge, with high melting points and vapour pressures, the non-metal remains in the solid state (Scheme 1). For  $X = \text{Sn}$ , which has very different physical properties and where Sn interacts considerably with the MW field itself, the situation is rather different and a range of possible reaction processes are possible, as discussed previously.<sup>5</sup>

Performing the  $\text{Mg}_2\text{X}$  MW syntheses under vacuum has profound effects on not only the way in which the reaction proceeds, but also on reaction efficiency and product purity. Comparing the purity of MIMP-synthesised  $\text{Mg}_2\text{Si}$  with that prepared using MW in the *solid state* in a nitrogen atmosphere under otherwise similar conditions previously (175 W, 120 s), the latter contained both Si and Mg as impurity phases among the products.<sup>36</sup> Given that the coupling of solid Si with the magnetic component of the field was proposed as the primary heating mechanism towards reaction with Mg, it is perhaps not unexpected that the products lacked homogeneity. By contrast, the study noted that the fine powdered Mg starting material did not couple effectively with either component of the 2.45 GHz MW field.<sup>36</sup>

In the MIMP reactions, the coupling and direct heating of both of the Mg and X reactant powders with MWs is clearly important and this is especially true for Mg, as the initial heating stage is the vital precursor to Mg plasma formation. This can be observed in the opening seconds of the MIMP reactions when from an initial state of no plasma formation, the colour of the evolving plasma transforms from purple (residual trace gas in the tube) to green (magnesium). This almost immediate and steady formation of reactant metal plasma *in vacuo* contributes hugely to the rapid reaction kinetics, as the motions of the charged particles in the plasma phase are enhanced by the 2.45 GHz electromagnetic field.<sup>3,5</sup> The possibility of producing  $\text{Mg}_2\text{X}$  ( $X = \text{Si, Ge, Sn}$ ) within 60 s contrasts enormously with equivalent conventional high-temperature solid-state approaches which typically require in excess of 10 h to complete.<sup>5,17</sup> While the results also demonstrate the powerful potential to fabricate bespoke nanostructured intermetallic materials *via* the



judicious selection of precursors, it will likely be the ability to scale up the MIMP method that will have the biggest impact on large scale materials production for applications such as rechargeable ion batteries and biomedical therapeutics.

## Conclusions

In summary, the MIMP approach has proved highly effective in the synthesis of the high purity, polycrystalline  $\text{Mg}_2\text{Si}$  and  $\text{Mg}_2\text{Ge}$  *Zintl* phases. Application of an incident power of merely 200 W to the solid elemental reactants *in vacuo*, led to each product within 60 s. The reaction of Mg with Ge was revealed as pseudomorphic, with nanoporous  $\text{Mg}_2\text{Ge}$  attainable from Mg powder and nanoporous Ge starting material. The experiments shed further light on the mechanisms of the MIMP process, demonstrating that the formation of metal (Mg) plasma is fundamental to its success. The plasma facilitates rapid reaction rates and the physical state of the other reactant, X, with which the plasma interacts, is pivotal in determining the microstructure of the products. The synthesis of high purity  $\text{Mg}_2\text{X}$  has also enabled further investigations of the structure–composition relationships of the silicide, germanide and stannide *Zintl* phases. The implications of Mg–Mg interactions within the  $\text{Mg}_8$  sub-lattices and the (non)existence of vacancies at the  $8c$  ( $1/4$ ,  $1/4$ ,  $1/4$ ) site are manifestly likely to be pivotal in determining the electronic (and possibly ionic) transport properties. Further systematic studies (including neutron diffraction combined with electrical and thermal conductivity measurements, for example) should be able to test these hypotheses further. Meanwhile, further investigations should be conducted to extend the MIMP method towards the rapid energy-efficient synthesis of other *Zintl* phases, intermetallics and alloys.

## Conflicts of interest

There are no conflicts to declare.

## Acknowledgements

DHG and ZF thank the University of Glasgow and the China Scholarship Council for the co-funding of a studentship for ZF. DHG thanks the Royal Society and EPSRC for associated funding under an International Exchange grant (IEC\R3\183040) and grant EP/N001982/1, respectively. W.-R. L. gratefully acknowledges the Ministry of Science and Technology, Taiwan, for support under project grants MOST 110-2923-E-006-011, 110-3116-F-011-002, 110-2622-E-033-009, 109-2911-I-033-502 and 108-E-033-MY3. ZF acknowledges the valuable experimental assistance and discussions from Dr. Mauro Davide Cappelluti (School of Chemistry, University of Glasgow). The authors acknowledge Mr. Cheng-Yi Lin (Department of Chemical Engineering, Chung Yuan Christian University) for assistance with SEM measurements.

## References

- 1 S. Maldonado, *ACS Energy Lett.*, 2020, 5(11), 3628–3632.
- 2 J. P. Siebert, C. M. Hamm and C. S. Birkel, *Appl. Phys. Rev.*, 2019, 6(4), 041314.
- 3 Z. Fan, G. Baranovas, A. Y. Holly, R. Szczęsny, W. R. Liu and D. H. Gregory, *Green Chem.*, 2021, 23(18), 6936–6944.
- 4 H. J. Kitchen, S. R. Vallance, J. L. Kennedy, N. Tapia-Ruiz, L. Carassiti, A. Harrison, A. G. Whittaker, T. D. Drysdale, S. W. Kingman and D. H. Gregory, *Chem. Rev.*, 2014, 114(2), 1170–1206.
- 5 Z. Fan, M. D. Cappelluti and D. H. Gregory, *ACS Sustainable Chem. Eng.*, 2019, 7(24), 19686–19698.
- 6 S. Chahal, S. M. Kauzlarich and P. Kumar, *ACS Mater. Lett.*, 2021, 3(5), 631–640.
- 7 S. Główniak, B. Szczęsniak, J. Choma and M. Jaroniec, *Adv. Mater.*, 2021, 33(48), 2103477.
- 8 S. R. Vallance, S. Kingman and D. H. Gregory, *Adv. Mater.*, 2007, 19(1), 138–142.
- 9 L. Carassiti, A. Jones, P. Harrison, P. S. Dobson, S. Kingman, I. MacLaren and D. H. Gregory, *Energy Environ. Sci.*, 2011, 4(4), 1503–1510.
- 10 S. Horikoshi, R. F. Schiffmann, J. Fukushima and N. Serpone, *Microwave Chemical and Materials Processing*, Springer, Singapore, 2018.
- 11 A. G. Whittaker and D. M. P. Mingos, *J. Chem. Soc., Dalton Trans.*, 1995, 2073–2079.
- 12 R. Santos, S. A. Yamini and S. X. Dou, *J. Mater. Chem. A*, 2018, 6(8), 3328–3341.
- 13 J. Tejada, M. Cardona, N. J. Shevchik, D. W. Langer and E. Schönherr, *Phys. Status Solidi B*, 1973, 58(1), 189–200.
- 14 B. Ryu, S. Park, E. Choi, J. D. Boor, P. Ziolkowski, J. Chung and S. D. Park, *J. Korean Phys. Soc.*, 2019, 75(2), 144–152.
- 15 A. Sankhla, A. Patil, H. Kamila, M. Yasseri, N. Farahi, E. Mueller and J. D. Boor, *ACS Appl. Energy Mater.*, 2018, 1(2), 531–542.
- 16 S. Yi, V. Attari, M. Jeong, J. Jian, S. Xue, H. Wang, R. Arroyave and C. Yu, *J. Mater. Chem. A*, 2018, 6(36), 17559–17570.
- 17 L. Zhang, Synthesis and thermoelectric properties of  $\text{Mg}_2\text{Si}$ – $\text{Mg}_2\text{Sn}$  solid solutions for waste heat recovery, *Doctoral dissertation*, The University of Texas at Austin, 2015.
- 18 W. Liu, X. Tan, K. Yin, H. Liu, X. Tang, J. Shi, Q. Zhang and C. Uher, *Phys. Rev. Lett.*, 2012, 108(16), 166601.
- 19 A. B. Ikhe, S. C. Han, S. J. R. Prabakar, W. B. Park, K. S. Sohn and M. Pyo, *J. Mater. Chem. A*, 2020, 8(28), 14277–14286.
- 20 D. T. Nguyen and S. W. Song, *J. Power Sources*, 2017, 368, 11–17.
- 21 H. Yaghoobnejad Asl, J. Fu, H. Kumar, S. S. Welborn, V. B. Shenoy and E. Detsi, *Chem. Mater.*, 2018, 30(5), 1815–1824.
- 22 W. An, B. Gao, S. Mei, B. Xiang, J. Fu, L. Wang, Q. Zhang, P. K. Chu and K. Huo, *Nat. Commun.*, 2019, 10(1), 1–11.
- 23 Y. An, Y. Tian, C. Wei, Y. Tao, B. Xi, S. Xiong, J. Feng and Y. Qian, *Nano Today*, 2021, 37, 101094.





- 24 Y. An, H. Fei, G. Zeng, L. Ci, S. Xiong, J. Feng and Y. Qian, *ACS Nano*, 2018, **12**(5), 4993–5002.
- 25 J. B. Cook, E. Detsi, Y. Liu, Y. L. Liang, H. S. Kim, X. Petrisans, B. Dunn and S. H. Tolbert, *ACS Appl. Mater. Interfaces*, 2017, **9**(1), 293–303.
- 26 J. Niu, H. Gao, W. Ma, F. Luo, K. Yin, Z. Peng and Z. Zhang, *Energy Storage Mater.*, 2018, **14**, 351–360.
- 27 H. Udono, H. Tajima, M. Uchikoshi and M. Itakura, *Jpn. J. Appl. Phys.*, 2015, **54**(7S2), 07JB06.
- 28 M. Sikora-Jasinska, P. Chevallier, S. Turgeon, C. Paternoster, E. Mostaed, M. Vedani and D. Mantovani, *RSC Adv.*, 2018, **8**(18), 9627–9639.
- 29 M. Ebrahimi, A. Zarei-Hanzaki, H. R. Abedi, M. Azimi and S. S. Mirjavadi, *Tribol. Int.*, 2017, **115**, 199–211.
- 30 M. Sikora-Jasinska, C. Paternoster, E. Mostaed, R. Tolouei, R. Casati, M. Vedani and D. Mantovani, *Mater. Sci. Eng., C*, 2017, **81**, 511–521.
- 31 C. Zhang, D. Ni, Y. Liu, H. Yao, W. Bu and J. Shi, *Nat. Nanotechnol.*, 2017, **12**(4), 378–386.
- 32 I. H. Kim, *J. Korean Phys. Soc.*, 2018, **72**(10), 1095–1109.
- 33 C. R. Clark, C. Wright, C. Suryanarayana, E. G. Baburaj and F. H. Froes, *Mater. Lett.*, 1997, **33**(1–2), 71–75.
- 34 S. C. Zhou and C. G. Bai, *Trans. Nonferrous Met. Soc. China*, 2011, **21**(8), 1785–1789.
- 35 S. Zhou and C. Bai, *J. Cent. South Univ.*, 2012, **19**(9), 2421–2424.
- 36 E. Savary, F. Gascoin and S. Marinel, *Dalton Trans.*, 2010, **39**(45), 11074–11080.
- 37 D. Berthebaud and F. Gascoin, *J. Solid State Chem.*, 2013, **202**, 61–64.
- 38 Y. G. Zhang, N. Du, C. M. Xiao, S. L. Wu, Y. F. Chen, Y. F. Lin, J. W. Jiang, Y. H. He and D. R. Yang, *RSC Adv.*, 2017, **7**, 33837–33842.
- 39 R. Saravanan and M. C. Robert, *J. Alloys Compd.*, 2009, **479**(1–2), 26–31.
- 40 H. E. Swanson, T. Eleanor and K. F. Ruth, *Natl. Bur. Stand. Circ.*, 1953, **539**, 1–95.
- 41 G. H. Grosch and K. J. Range, *J. Alloys Compd.*, 1996, **235**(2), 250–255.
- 42 A. S. Cooper, *Acta Crystallogr.*, 1962, **15**(6), 578–582.
- 43 D. M. Többsens, N. Stüßner, K. Knorr, H. M. Mayer and G. Lampert, *Mater. Sci. Forum*, 2001, **378**, 288–293.
- 44 S. Sasaki, K. Fujino and Y. Takéuchi, *P. JPN Acad. B*, 1979, **55**(2), 43–48.
- 45 B. H. Toby, *J. Appl. Crystallogr.*, 2001, **34**(2), 210–213.
- 46 K. Momma and F. Izumi, *J. Appl. Crystallogr.*, 2011, **44**(6), 1272–1276.
- 47 T. Dasgupta, C. Stiewe, R. Hassdorf, A. J. Zhou, L. Boettcher and E. Mueller, *Phys. Rev. B: Condens. Matter Mater. Phys.*, 2011, **83**(23), 235207.
- 48 K. Yin, Q. Zhang, Y. Zheng, X. Su, X. Tang and C. Uher, *J. Mater. Chem. C*, 2015, **3**(40), 10381–10387.
- 49 J. Liang, X. Li, Z. Hou, C. Guo, Y. Zhu and Y. Qian, *Chem. Commun.*, 2015, **51**(33), 7230–7233.
- 50 K. Sekino, M. Midonoya, H. Udono and Y. Yamada, *Phys. Procedia*, 2011, **11**, 171–173.
- 51 L. Umaralikhan and M. Jamal Mohamed Jaffar, *Iran. J. Sci. Technol.*, 2018, **42**(2), 477–485.
- 52 H. Mizoguchi, Y. Muraba, D. C. Fredrickson, S. Matsuishi, T. Kamiya and H. Hosono, *Angew. Chem., Int. Ed.*, 2017, **56**, 10135–10139.
- 53 E. Sanville, S. D. Kenny, R. Smith and G. Henkelman, *J. Comput. Chem.*, 2007, **28**, 899–908.
- 54 M. Brause, B. Braun, D. Ochs, W. Maus-Friedrichs and V. Kempter, *Surf. Sci.*, 1998, **398**(1–2), 184–194.
- 55 M. R. J. V. Buuren, F. Voermans and H. V. Kempen, *J. Phys. Chem.*, 1995, **99**, 9519–9522.
- 56 C. R. Whitsett, *Electrical properties of magnesium silicide and magnesium germanide*, Iowa State University, 1955.
- 57 Y. Zhang, N. Du, C. Xiao, S. Wu, Y. Chen, Y. Lin, J. Jiang, Y. He and D. Yang, *RSC Adv.*, 2017, **7**(54), 33837–33842.
- 58 H. Hosono and M. Kitano, *Chem. Rev.*, 2021, **121**(5), 3121–3185.
- 59 M. Kubouchi, K. Hayashi and Y. Miyazaki, *J. Alloys Compd.*, 2014, **617**, 389–392.
- 60 S. S. Batsanov, *Russ. Chem. Bull.*, 1995, **44**(12), 2245–2250.
- 61 J. Ahn, B. Kim, G. Jang and L. Moon, *ChemElectroChem*, 2018, **5**(19), 2729–2733.
- 62 M. Saruyama, R. Sato and T. Teranishi, *Acc. Chem. Res.*, 2021, **54**, 765–775.

